

Extracting Blood Vessels From Full-Field OCT Data of Human Skin by Short-Time RPCA

Pin-Hsien Lee^{ID}, Chin-Cheng Chan, Sheng-Lung Huang^{ID},
Andrew Chen, and Homer H. Chen^{ID}, *Fellow, IEEE*

Abstract—Recent advances in optical coherence tomography (OCT) lead to the development of OCT angiography to provide additional helpful information for diagnosis of diseases like basal cell carcinoma. In this paper, we investigate how to extract blood vessels of human skin from full-field OCT (FF-OCT) data using the robust principal component analysis (RPCA) technique. Specifically, we propose a short-time RPCA method that divides the FF-OCT data into segments and decomposes each segment into a low-rank structure representing the relatively static tissues of human skin and a sparse matrix representing the blood vessels. The method mitigates the problem associated with the slow-varying background and is free of the detection error that RPCA may have when dealing with FF-OCT data. Both short-time RPCA and RPCA methods can extract blood vessels from FF-OCT data with heavy speckle noise, but the former takes only half the computation time of the latter. We evaluate the performance of the proposed method by comparing the extracted blood vessels with the ground truth vessels labeled by a dermatologist and show that the proposed method works equally well for FF-OCT volumes of different quality. The average F-measure improvements over the correlation-mapping OCT method, the modified amplitude-decorrelation OCT angiography method, and the RPCA method, respectively, are 0.1835, 0.1032, and 0.0458.

Index Terms—Robust principal component analysis, optical coherence tomography, blood vessel detection.

Manuscript received December 22, 2017; revised March 28, 2018 and April 30, 2018; accepted May 1, 2018. Date of publication May 8, 2018; date of current version July 31, 2018. This work was supported by the Ministry of Science and Technology of Taiwan under Grant 106-2221-E-002-201-MY3 and Grant 107-2634-F-002-017. (Corresponding author: Homer H. Chen.)

P.-H. Lee is with the Graduate Institute of Communication Engineering, National Taiwan University, Taipei 10617, Taiwan (e-mail: r04942041@ntu.edu.tw).

C.-C. Chan is with the Department of Electrical Engineering, National Taiwan University, Taipei 10617, Taiwan (e-mail: b03901057@ntu.edu.tw).

S.-L. Huang is with the Department of Electrical Engineering, Graduate Institute of Photonics and Optoelectronics, National Taiwan University, Taipei 10617, Taiwan (e-mail: shuang@ntu.edu.tw).

A. Chen is with the Flaum Eye Institute, University of Rochester School of Medicine & Dentistry, Rochester, NY 14642 USA (e-mail: andrew_chen@urmc.rochester.edu).

H. H. Chen is with the Department of Electrical Engineering, the Graduate Institute of Communication Engineering, and the Graduate Institute of Networking and Multimedia, National Taiwan University, Taipei 10617, Taiwan (e-mail: homer@ntu.edu.tw).

Color versions of one or more of the figures in this paper are available online at <http://ieeexplore.ieee.org>.

Digital Object Identifier 10.1109/TMI.2018.2834386

I. INTRODUCTION

OPTICAL coherence tomography (OCT) is a biomedical optical imaging technique that enables non-invasive, high-resolution imaging of the underlying structure of biological tissue [1]–[3]. Due to the advances of lighting and detection techniques, OCT has significantly improved in many aspects: micron-scale resolution at or near the cellular level, high imaging speed up to millions of A-scans per second, high sensitivity, and functionality extensions [3]. It has become integral to ophthalmic diagnosis and management of retinal diseases and is a burgeoning topic in other medical fields, such as dermatology, cardiology, and neurology. In this paper, we focus on the detection of blood vessel from OCT data of human skin.

Recent studies suggest that blood flow anomalies provide relevant information for diagnosis of skin diseases, such as basal cell carcinoma [5] and psoriasis [6], [7]. OCT imaging allows not only the structure, but also the blood flow of a biological tissue to be captured. Optical coherence tomography angiography (OCTA) [4], [20], [21] is one such technique that extracts the vascular network in a biological tissue from the OCT data. In clinical practices, its use is rapidly expanding for diseases such as diabetic retinopathy and other retinal vascular diseases because it provides a level of detail that far exceeds that obtained with older forms of blood flow imaging. In general, OCTA methods can be classified into three categories: phase-based, amplitude-based, and complex-based. Phase-based OCTA evaluates the phase shift resulting from blood flow to delineate blood vessels and thus requires the OCT to provide high phase stability or high resistance to phase noise caused by tissue motion [19]. Amplitude-based OCTA does not suffer from phase noise and is able to work with OCT data without phase information. Complex-based OCTA analyzes both phase and amplitude in OCT data [33], [34].

We propose a new amplitude-based OCTA method that extracts blood vessels of human skin from full-field OCT (FF-OCT) data. Most other amplitude-based methods are based on the correlation between consecutive images in OCT data. Such methods are sensitive to speckle noise and the slight image variation along the axial direction of FF-OCT. The image variation is typical to the FF-OCT data because each *en face* image represents a different layer of human skin. To improve the robustness to speckle noise,

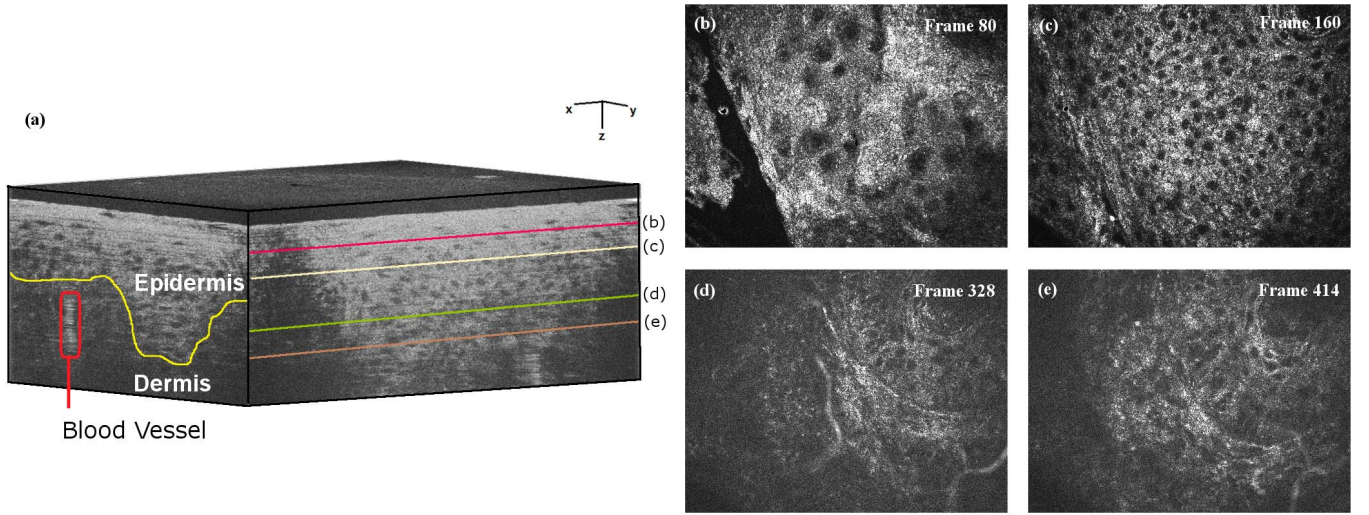


Fig. 1. A sample FF-OCT data of *in vivo* human skin. This sample is taken from a 25-year-old male subject. (a) 3-D view of an example skin FF-OCT data. The dermis-epidermis junction is labeled in yellow curve, and the vessel is marked with red circle. (b) and (c) Two *en face* slices of epidermis. (d) and (e) Two *en face* slices of dermis. Each *en face* slice has a size of 488×648 pixels, representing a 220×290 micron square in dimension.

we adopt the technique called robust principle component analysis (RPCA) [22]–[24] and represent the relatively static tissues of human skin by a low-rank structure and the blood vessels by a sparse matrix. To reduce the sensitivity of RPCA to image variation along the axial direction of FF-OCT, we incorporate the idea of short-time¹ analysis into RPCA. The basic concept of this work was presented earlier in a conference [29]; this paper provides a more thorough evaluation of the performance of the proposed method.

The remainder of this paper is organized as follows. The FF-OCT and previous OCTA methods are reviewed in Section II. The proposed method for blood vessel detection from FF-OCT data of human skin is described in Section III, and the experimental results are described in Section IV. Finally, we conclude our work in Section V.

II. BACKGROUND

OCT is based on low-coherence interferometry to obtain images of the structure of live biological tissue [2]. Specifically, the interference pattern of one sample tissue is obtained by combining the light beam reflected from the tissue and that from the reference mirror inside the OCT system. By analyzing the interference pattern, the magnitude and time delay of the reflected light from the tissue can be obtained. The longitudinal position of the reflection sites indicates the anatomical structure of the sample tissue.

The FF-OCT system we used to acquire the 3-D OCT data records 2-D transverse slices, referred to as *en face* images, and builds them up along the axial direction to construct a 3-D volume [8], [9]. In general, FF-OCT has two advantages over OCT [3]. First, it is free of the artifact caused by the bulk motion of the tissue along the two transverse directions. Although most commercial OCT systems are fast and can

acquire a 3-D OCT volume in just a few seconds, the motion of the sample tissue introduces spatial discontinuity to each 2-D slice of the OCT volume, resulting in the motion artifact. Our FF-OCT system simultaneously acquires all pixels in an *en face* image by a 2-D camera and hence can limit the discontinuity to the axial direction only. Second, it achieves better sensitivity than OCT because an *en face* image in FF-OCT has a longer exposure than a slice in OCT.

Our Mirau-based FF-OCT system [10] has an axial and lateral (i.e. transverse) resolution of $0.9 \mu\text{m}$ and $0.8 \mu\text{m}$, respectively. The light source is a cerium-doped yttrium aluminum garnet single-clad crystal fiber that emits broadband light with the center wavelength of 560 nm and a bandwidth of 95 nm . The objective at the sample arm is a home-designed silicone-oil-immersion Mirau objective with a NA of 0.8 . The scan speed of *en face* images is 4.3 frames per second.

Fig. 1 shows a volume of data generated from our FF-OCT system. The volume of data shown in Fig. 1(a) reveals the structure of a face skin tissue from a 25-year-old Asian male subject, with a frame separation of $0.2 \mu\text{m}$. Each *en face* image in the volume has a size of 488×648 pixels, representing a 220×290 micron square in physical dimension. Figs. 1(b) and 1(c) show the *en face* images of epidermis, and Figs. 1(d) and 1(e) show the *en face* images of dermis, where the blood vessel network resides. The frame number of each image indicates the chronological order captured by the FF-OCT system. The larger the frame number, the deeper the tissue. Our FF-OCT system has a sub-micron resolution and can detect capillaries around $5 \mu\text{m}$ in diameter. Fig. 2 shows some examples of red blood cells in different *en face* images. The red blood cells constitute the white clusters in the dermis layer. Extracting blood vessels in the FF-OCT volume data is made possible by detecting these red blood cells.

Visualization of the blood flow of a biological tissue is a major research topic for OCT and has an important implication

¹Here, we follow the convention and call it short-time analysis. But the time axis in this context actually refers to the axial direction of FF-OCT.

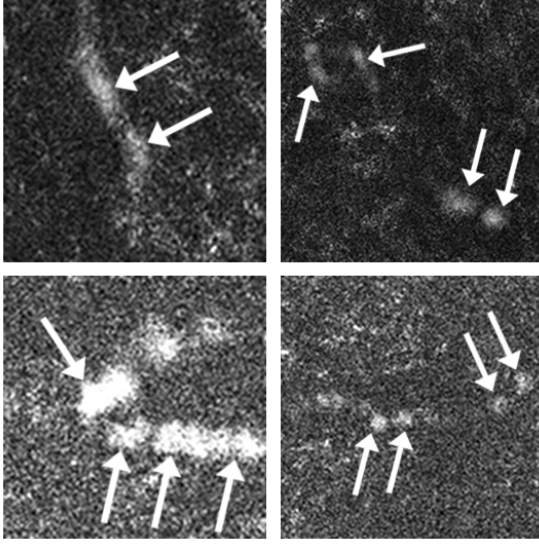


Fig. 2. Red blood cells in four different skin FF-OCT *en face* images. Bright clusters pointed by arrows are the red blood cells. These moving cells show the location of blood vessels in the live skin tissue.

for clinical diagnosis. For example, skin diseases such as basal cell carcinoma cause changes in the vasculature of the skin lesion, which can be observed in and diagnosed with the OCT volume [5]–[7]. Approaches to visualization of blood flow in a biological tissue can be roughly divided into two categories: Doppler OCT (DOCT) and OCTA. However, more refined approaches have been proposed to isolate vessels better, for example, by combining phase and amplitude information [30]. Structural analysis and weighted speckle parameters have also been utilized [31]. The Doppler OCT has high sensitivity to axial motion and hence requires high-performance phase compensation algorithm to isolate blood flow from bulk tissue motions. On the other hand, the OCTA, although less sensitive to particle motions, can extract the transverse blood flow of a biological tissue without such phase compensation algorithm and is more suitable for imaging the microvasculature of human skin. Several OCTA methods have been proposed in recent years [14]–[19]. As described in Section I, there are three kinds of OCTA methods for visualization: phase-based, amplitude-based, and complex-based [20], [21], [33], [34]. The FF-OCT volume acquired by our Mirau-based FF-OCT system loses the phase information once the Hilbert transform is applied [10]. Thus, we only review the amplitude-based OCTA methods here.

Enfield *et al.* [17] introduced the correlation mapping optical coherence tomography (cmOCT) technique to extract blood vessels from a volume of OCT images and reported that the OCT image regions corresponding to blood vessels tend to have a lower cross-correlation between consecutive images than the relatively static background regions. The cmOCT technique does not require phase information; therefore, it can be applied to FF-OCT data as well [18]. Jia *et al.* [19] developed the split-spectrum amplitude-decorrelation angiography that reduces the motion artifact along the axial direction while preserving the transverse blood flow. Unlike its split-spectrum counterpart,

the full-spectrum amplitude-decorrelation angiography does not require phase information. Thus it can be applied to FF-OCT data [21].

As a variant of the principal component analysis, RPCA has been developed to separate a static background from moving objects, which are considered as outliers. While the principal component analysis is sensitive to gross outliers, RPCA models the outliers as a sparse matrix so that the principal components of the static background can be properly extracted. In surveillance applications, for example, this means one may model the static scene (background) as a low-rank matrix and the moving objects (foreground) as a sparse matrix so that the foreground can be properly separated from the background [28].

III. METHOD

In light of its strength for background subtraction, the RPCA technique is employed in the proposed method to extract blood vessels from FF-OCT data. The red blood cells, which are sparsely distributed in the *en face* images, move in the blood vessels while other parts of the skin tissue remain nearly static across consecutive *en face* images. Therefore, the red blood cells can be considered as foreground and the other parts of the skin tissue as background.

In a typical RPCA formulation, the background is modeled as a low-rank matrix and the foreground as a sparse matrix. Using this formulation, we vectorize each *en face* image and represent the entire FF-OCT volume as a 2-D matrix. Then, we decompose the matrix into a low-rank matrix representing the relatively static part of the skin tissue and a sparse matrix representing the blood vessels.

Suppose that an FF-OCT volume of data is composed of k *en face* images of the size $m \times n$. By turning each *en face* image into a vector and stacking all such vectors, we obtain an $mn \times k$ matrix D and turn the blood vessel detection into an optimization problem,

$$\min_{\mathbf{A}} \text{rank}(\mathbf{A}) + \lambda \|\mathbf{E}\|_0, \quad \text{s.t. } \mathbf{D} = \mathbf{A} + \mathbf{E}, \quad (1)$$

where A denotes the low-rank matrix representing the static parts of skin tissue, $\text{rank}(\cdot)$ denotes the rank operator, E denotes the sparse matrix representing the red blood cells, and λ denotes a penalty factor that controls the number of non-zero values in E and ultimately the quality of the extracted blood vessels.

The optimization problem (1) is NP-hard [22]. Wright *et al.* [23] relaxed the rank constraint to the nuclear norm and the sparsity constraint to l_1 -norm and turned (1) into a convex optimization problem,

$$\min_{\mathbf{A}} \|\mathbf{A}\|_* + \lambda \|\mathbf{E}\|_1, \quad \text{s.t. } \mathbf{D} = \mathbf{A} + \mathbf{E}, \quad (2)$$

where $\|\cdot\|_*$ denotes the nuclear norm of a matrix. Among the algorithms that have been proposed to solve (2), we choose the inexact augmented Lagrange multiplier method [24] because it is computationally efficient. The procedure of this method is summarized in Algorithm 1, where the element-wise shrinkage operator $S(\cdot, \cdot)$ is defined as follows:

$$S(\mathbf{X}, \varepsilon) = \text{sgn}(\mathbf{X}) \max(|\mathbf{X}| - \varepsilon, 0). \quad (3)$$

Algorithm 1 Inexact Augmented Lagrange Multiplier Solver

Input: An FF-OCT data \mathbf{D} and the sparsity penalty λ .

```

1:  $\mathbf{Y}_0 = \mathbf{D} / \max(\|\mathbf{D}\|_2, \|\mathbf{D}\|_\infty / \lambda)$ .
2:  $\mathbf{A}_0 = \mathbf{0}$ ;  $\mathbf{E}_0 = \mathbf{0}$ ;  $\mu_0 > 0$ ;  $\rho > 1$ ;  $k = 0$ .
3: while not converged do
4:    $(\mathbf{U}, \Sigma, \mathbf{V}) = \text{svd}(\mathbf{D} - \mathbf{E}_k + \mathbf{Y}_k / \mu_k)$ .
5:    $\mathbf{A}_{k+1} = \mathbf{US}(\Sigma, 1/\mu_k)\mathbf{V}^T$ .
6:    $\mathbf{E}_{k+1} = \mathbf{S}(\mathbf{D} - \mathbf{A}_{k+1} + \mathbf{Y}_k / \mu_k, \lambda / \mu_k)$ .
7:    $\mathbf{Y}_{k+1} = \mathbf{Y}_k + \mu_k(\mathbf{D} - \mathbf{A}_{k+1} - \mathbf{E}_{k+1})$ .
8:    $\mu_{k+1} = \rho \mu_k$ .
9:    $k = k + 1$ .
10: end while

```

Output: The low-rank matrix \mathbf{A} and the sparse matrix \mathbf{E} .

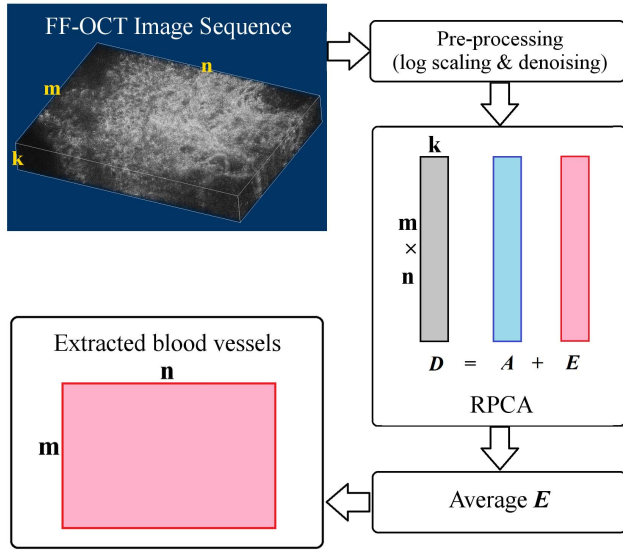


Fig. 3. Flowchart of the RPCA method. The FF-OCT volume is reshaped into a 2-D matrix and processed by the RPCA algorithm. Red blood cells are classified as sparse matrix \mathbf{E} , and the average of \mathbf{E} represents the extracted blood vessels.

The flowchart of the RPCA method is shown in Fig. 3. We perform two pre-processing steps on the FF-OCT volume of data before solving (2). The first step is a logarithmic scaling operation that attenuates the high responses caused by melanin while preserving the shape of blood cell in the raw data [11]. The second step is a speckle noise reduction operation. The speckle noise affects the contrast of OCT images and degrades blood vessel detection; therefore, we use a median filter with a window size of 7×7 (determined empirically) to remove the speckle noise.

The RPCA serves as the theoretical foundation for our blood vessel detection algorithm. However, when dealing with the FF-OCT data in which the background varies slightly from image to image, it does not perform as expected. This is because that each *en face* image represents a different layer of the skin tissue. The column vectors of \mathbf{A} , which represent the static part of skin tissue, are not uniform due to the slight variation in background from one image to another along the axial direction. Although the difference between the consecutive vectors of \mathbf{A} is small, the accumulation over

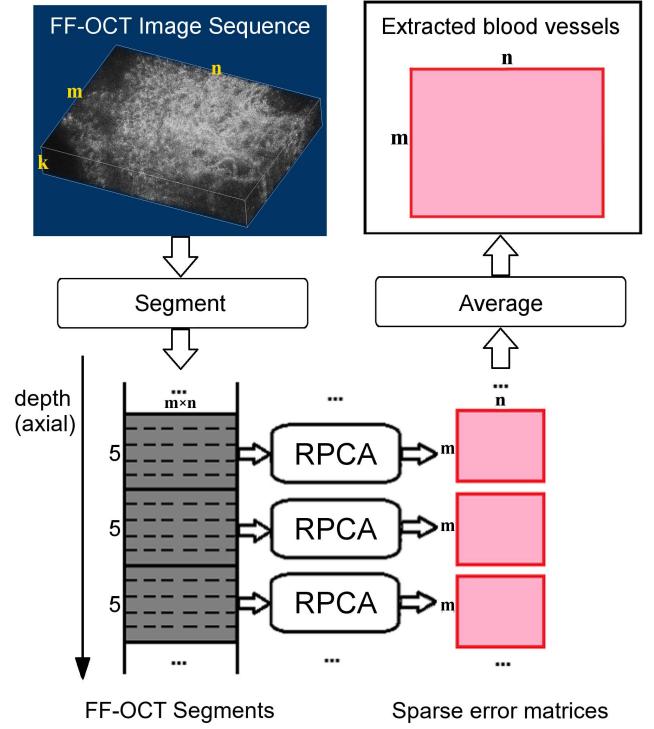


Fig. 4. Flowchart of the short-time RPCA method. The FF-OCT volume is partitioned into small segments of equal length. The average of the sparse matrices of all segments is considered the extracted blood vessels.

the whole volume has a profound impact on the quality of the extracted blood vessels. Several attempts have been made to address the issue [25]–[27], but most of them involve a complex RPCA formulation that is computationally inefficient.

We propose a simple but effective method called short-time RPCA to cope with the slight variation of background in FF-OCT data. It entails the partitioning of the original data into small segments of equal length, and application of the RPCA method to each segment. Here, each segment consists of a number of consecutive *en face* images and forms the input \mathbf{D} in (2). Since the background within the short-time interval has a low-rank structure, the short-time RPCA method does not suffer much from the variation of background. Assume that each segment consists of κ *en face* images. The cost of the short-time RPCA method is of the order of $O(k/\kappa \times mn\kappa^2) = O(mn\kappa\kappa)$, while that of the RPCA method is of the order of $O(mn\kappa^2)$ [28]. Because κ is much smaller than k , the short-time RPCA method has less computational complexity than the RPCA method and hence takes less computation time (Section IV.F).

The flowchart of the proposed short-time RPCA method is depicted in Fig. 4. The short-time RPCA has the best detection accuracy when κ is in the range [2,9], and we choose $\kappa = 5$ for all data in the following experiments. Every five consecutive *en face* images in an FF-OCT volume of data are grouped together to form a segment that is $1 \mu\text{m}$ in depth. The sparse matrix of a segment consists of five columns, each of which represents the detected blood vessels in an *en face* image. The average of the five columns is taken as the output of the segment. Then, we take the average of the outputs of all segments to generate the final blood vessel image. Algorithm 2

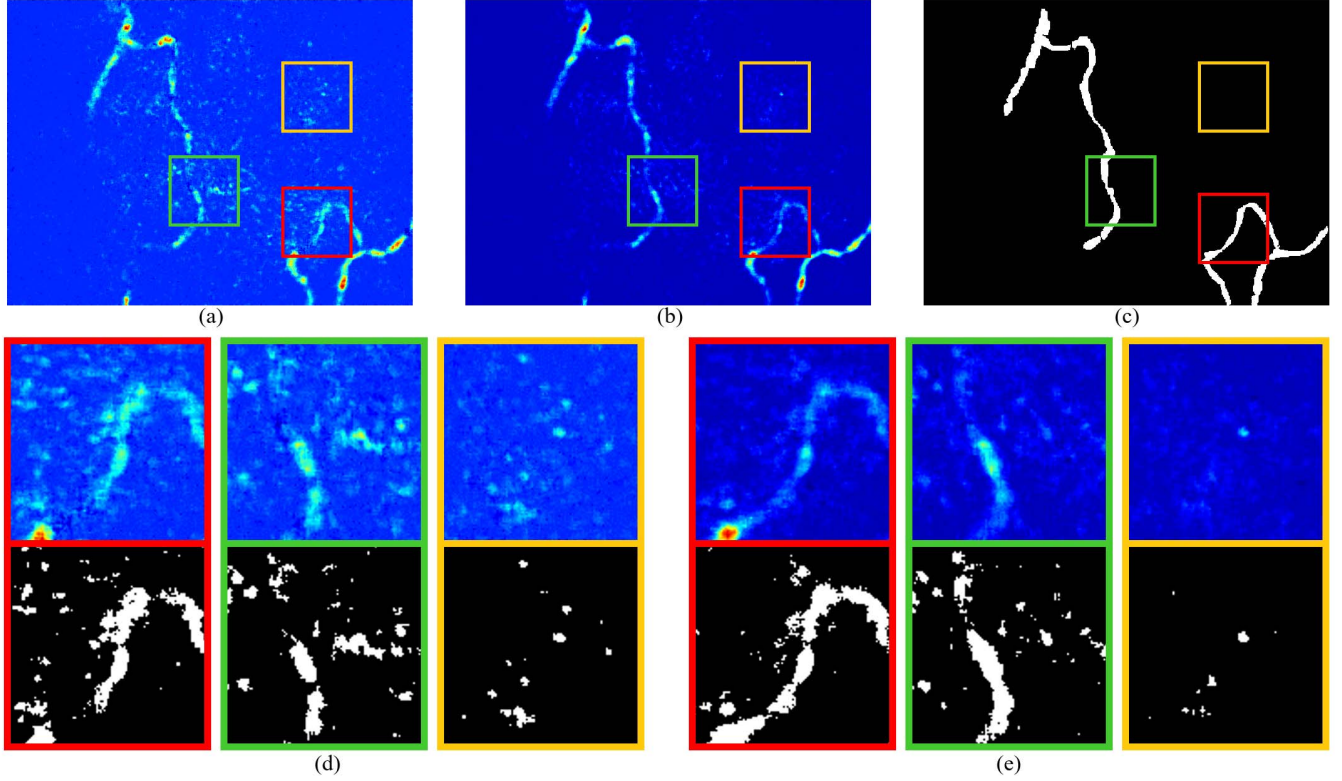


Fig. 5. Blood vessels extracted by (a) RPCA and (b) short-time RPCA. (c) Ground truth blood vessels. (d) and (e) shows detailed visualization in red, green, and orange boxes in (a) and (b), respectively.

summarizes the procedure of the proposed short-time RPCA method.

Algorithm 2 Short-Time RPCA

Input: The FF-OCT volume \mathbf{D} , the sparsity penalty λ , and the segment length κ .

- 1: Segment \mathbf{D} into segments with length of κ .
- 2: **for each** segment \mathbf{D}_i
- 3: $(\mathbf{E}_i, \mathbf{A}_i) = \text{Inexact_ALM}(\mathbf{D}_i, \lambda)$.
- 4: Compute \mathbf{M}_i , the average of \mathbf{E}_i along the axial direction.

5: **end for**

6: Compute \mathbf{B} , the average of \mathbf{M} .

Output: Detected blood vessels \mathbf{B}

Figs. 5(a) and 5(b) show the blood vessels extracted by the RPCA and the short-time RPCA methods, respectively, and Figs. 5(d) and 5(e) show the zoom-in images of blood vessels. The short-time RPCA has less false detections than the RPCA, and the extraction of the former looks more like the ground truth blood vessels shown in Fig. 5(c).

IV. EXPERIMENTS

We conducted experiments to evaluate the performance of the proposed short-time RPCA method against other methods for blood vessel detection. The extracted blood vessels are visually inspected and compared with ground truth in terms of accuracy. In addition, we tested how the sparsity penalty

TABLE I
ATTRIBUTES OF SUBVOLUMES USED IN EXPERIMENTS

Subvolume Number	Source Volume	First and Last Frames	CNR (mean \pm s.d.)
1	V_1	251–350	12.70 ± 1.33
2	V_1	351–450	12.27 ± 1.07
3	V_1	451–550	10.28 ± 1.04
4	V_2	251–350	10.43 ± 1.68
5	V_2	351–450	9.64 ± 0.91
6	V_2	451–550	8.28 ± 0.51
7	V_3	251–350	13.19 ± 3.52
8	V_3	351–450	9.24 ± 1.41
9	V_3	451–550	8.39 ± 0.69
10	V_4	251–350	13.33 ± 2.96
11	V_4	351–450	10.57 ± 0.90
12	V_4	451–550	9.33 ± 0.84
13	V_5	301–400	7.79 ± 1.06
14	V_5	401–500	7.61 ± 0.57
15	V_6	299–398	8.01 ± 0.67

factor λ affects the quality of extracted blood vessels of the short-time RPCA.

A. Description of Experiments

We scanned human forearm and face to obtain six different volumes of FF-OCT data. The six volumes were acquired independently, each took about two minutes. Each volume consists of 550 *en face* images with a resolution of 488×648 and is 100 μm deep. Among the six volumes, a total of 15 subvolumes (see Table I for details) were found to

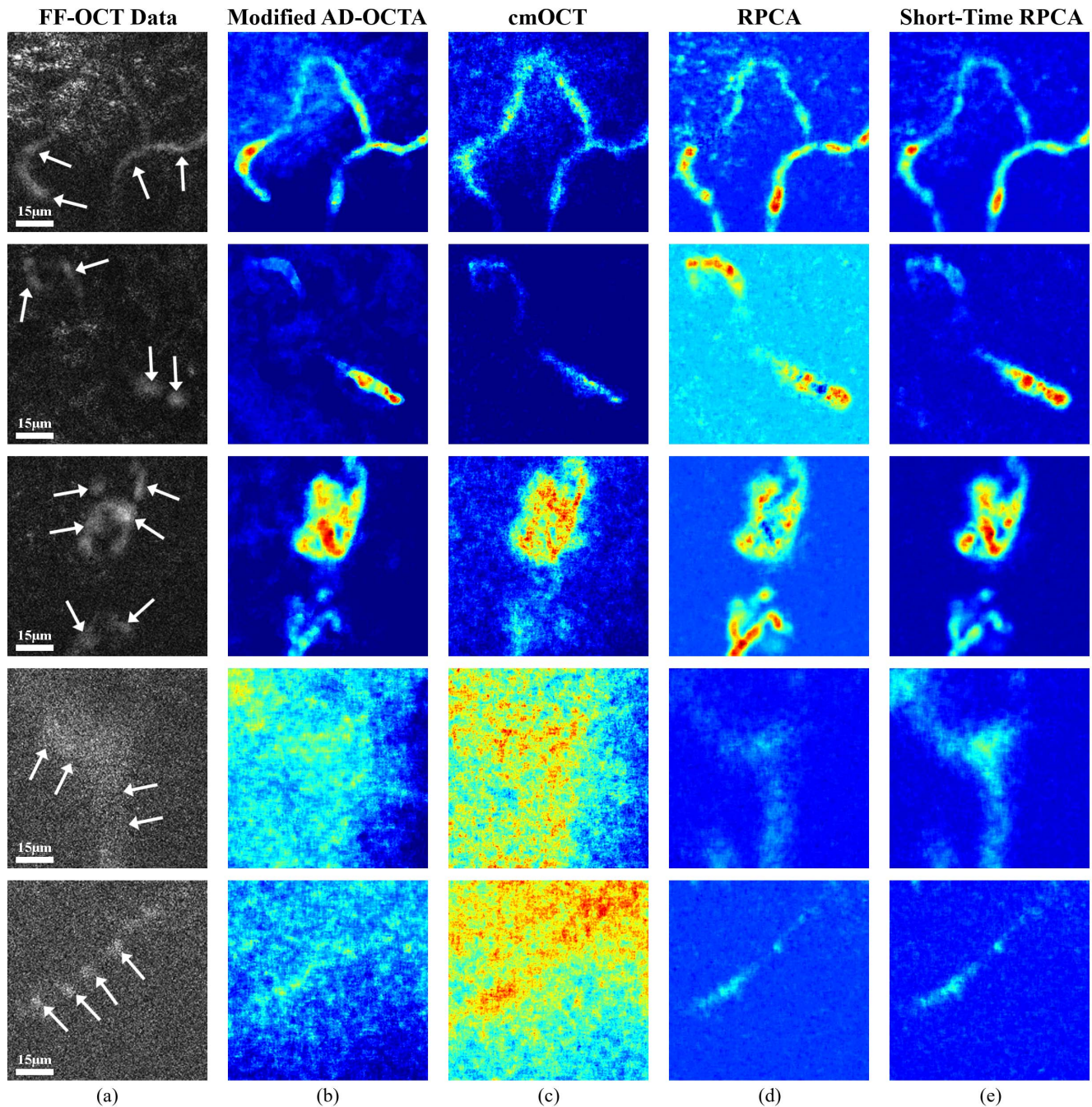


Fig. 6. Blood vessels extracted by modified AD-OCTA, cmOCT, RPCA, and short-time RPCA. Each row represents an FF-OCT subvolume. Five subvolumes from top to bottom are 2, 4, 11, 9, and 15, respectively. (a) An example *en face* image. Bright clusters pointed by arrows are red blood cells, and regions occupied by red blood cells represent blood vessels. (b) Result of the modified AD-OCTA method. (c) Result of the cmOCT method. (d) Result of the RPCA method. (e) Result of the short-time RPCA method.

contain blood vessels and retained for blood vessel extraction. Each subvolume contains 100 *en face* images in the dermis layer and physically covers an area of $220 \times 290 \mu\text{m}^2$ and a depth of $20 \mu\text{m}$.

The scan speed of the Mirau-based FF-OCT system is adjustable; in the last two volumes (i.e. V_5 and V_6), the system scan speed is doubled (8.6 frames/sec instead of 4.3 frames/sec). With a higher scan speed, the system takes less interferometric images to do averaging while

generating an *en face* image. This results in more speckle noise in FF-OCT data, making blood vessel extraction harder.

We evaluated our method against three other methods: amplitude-decorrelation OCTA (AD-OCTA) [19], [21], correlation-mapping OCT (cmOCT) [17], and RPCA. When we first started the experiment, both preprocessing steps were applied to all three methods under comparison. However, we found that cmOCT produced worse results—more false blood vessels—with the median filter. Apparently, removing

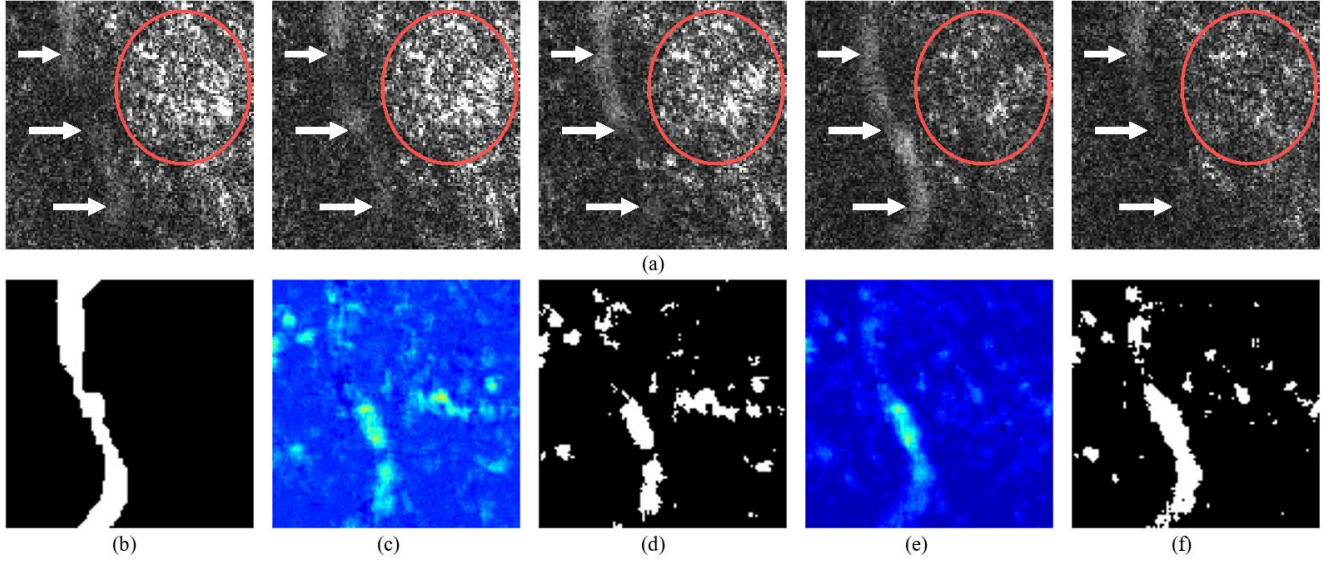


Fig. 7. Illustration of the performance of blood vessel detection in the presence of melanin granules. (a) Five consecutive *en face* images of Subvolume 2. Red blood cells are pointed to by white arrows, and melanin particles are enclosed by red circles. (b) Ground truth blood vessel. (c) Result of the RPCA method. (d) Binarized result of the RPCA method. (e) Result of the short-time RPCA method. (f) Binarized result of the short-time RPCA method.

the speckle noise affects the correlation between *en face* images. Therefore, we decided not apply it to cmOCT. To apply both AD-OCTA and cmOCT to FF-OCT data, we performed the following steps:

1) **Modified AD-OCTA**: The AD-OCTA method was developed to process 4-D OCT data with N cross-sectional images (B-scans) at the same lateral location but different time. Each pair of two consecutive B-scans is associated with a decorrelation (angiography) image. The blood vessel image at the lateral location is the average of all $N - 1$ decorrelation images.

The FF-OCT system used in this work does not perform repetitive scanning at a fixed lateral or axial location. To make the data compatible with the input format of the AD-OCTA method, we partitioned each subvolume into small segments and considered that all *en face* images in a segment are acquired at almost the same axial location. This is a reasonable treatment because the five *en face* images of each segment have a depth of only $1.0 \mu\text{m}$, which means the static tissue parts in all five *en face* images are almost identical. We calculated the blood vessel image of each segment and took the average of all images as the blood vessel image of the subvolume.

2) **cmOCT**: To apply the cmOCT method to the FF-OCT data, we computed a 2-D correlation image C from two consecutive *en face* images. Each pixel value of C is the Pearson correlation coefficient of two blocks, one from each image, that are centered at the pixel and have a size of 3×3 . An image block of the static tissue has a positive Pearson correlation coefficient; therefore, we assigned -1 (meaning background) to the corresponding pixel of C . This way, a total of 99 correlation images were generated for each subvolume, and the average of all correlation images was taken as the blood vessel image of the subvolume.

B. Evaluation Metrics

The binary blood vessel image generated by each method is compared with the ground truth blood vessel image labeled by a dermatologist. The dermatologist marked all red blood cells in every *en face* image of all subvolumes. For each subvolume, a total of 100 binary images were generated, and the union of all binary images was taken as the ground truth blood vessel image of the subvolume.

We computed the precision and recall scores of a binary blood vessel image as follows:

$$\text{Precision} = \frac{T_p}{T_p + F_p}, \quad (4)$$

$$\text{Recall} = \frac{T_p}{T_p + F_n}, \quad (5)$$

where T_p , F_p , and F_n , respectively, are the number of true positives, false positives, and false negatives of the binary blood vessel image. To evaluate the detection accuracy of a method, we used the F-measure that combines precision and recall:

$$\text{F-measure} = 2 \frac{\text{Precision} \cdot \text{Recall}}{\text{Precision} + \text{Recall}}. \quad (6)$$

The higher the F-measure, the better the detection accuracy.

To define the contrast-to-noise ratio (CNR) for an *en face* image, we consider the ground truth blood vessel region as signal and the pixels with the bottom 10% intensity as noise. Then, the CNR of an *en face* image can be expressed as

$$\text{CNR} = \frac{\bar{I}_v - \bar{I}_n}{\sigma_n}, \quad (7)$$

where \bar{I}_v , \bar{I}_n , respectively, are the mean intensity values of the blood vessel region and the noise region, and σ_n is the standard deviation of the noise. We evaluate the image quality

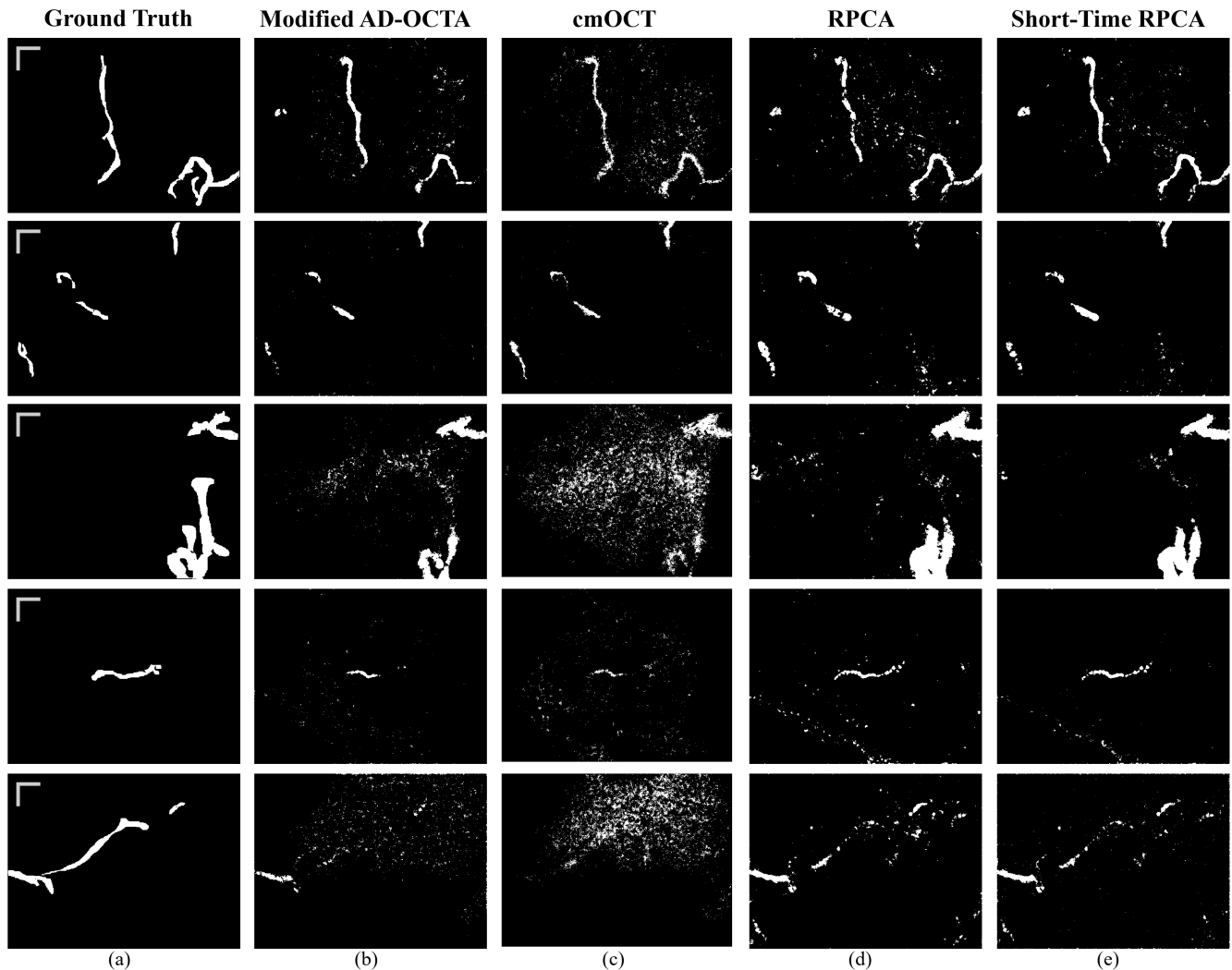


Fig. 8. The ground truth blood vessels vs. the binary blood vessels generated by modified AD-OCTA, cmOCT, RPCA, and short-time RPCA. Five subvolumes from top to bottom are 1, 4, 8, 13, and 15, respectively. (a) Ground truth. The scale bar represents 30 μm . (b) The modified AD-OCTA method. (c) The cmOCT method. (d) The RPCA method. (e) The proposed short-time RPCA method.

of a subvolume by mean CNR, which is the average of all CNR values of 100 *en face* images of the subvolume. Table I lists the mean CNR of all subvolumes. It can be found that the deeper the subvolume, the lower the mean CNR.

C. Comparison Based on Extracted Blood Vessels

Fig. 6(a) shows example images of five FF-OCT subvolumes. Figs. 6(b) to 6(e), in order, show the blood vessels extracted by the modified AD-OCTA, the cmOCT, the RPCA, and the short-time RPCA methods. Zoom-in images are shown for visualization of details. For comparison purpose, we separate the five subvolumes in Fig. 6 into two groups: high mean CNR and low mean CNR.

1) *High-Mean-CNR Subvolumes*: The top three rows of Fig. 6 have a mean CNR of 12.27, 10.43, and 10.57, respectively. Because the subvolumes have high image quality, all four methods are able to extract blood vessels. However, the short-time RPCA provides the cleanest contrast between the blood vessels and the background. In addition, the blood

vessel images generated by the short-time RPCA have fewer false detections than those by the RPCA.

2) *Low-Mean-CNR Subvolumes*: The bottom two rows of Fig. 6 have a low mean CNR. From top to bottom, the mean CNR is 8.39 and 8.01, respectively. It can be seen that both modified AD-OCTA and cmOCT fail to detect the blood vessels in the subvolumes because they are sensitive to the speckle noise in FF-OCT data. On the other hand, both RPCA and short-time RPCA are able to detect at least the main body of the blood vessels.

During *in vivo* experiments, artifact from patient breathing or local blood flow can alter the melanin distribution in a subvolume. These tiny movements can be detected by an RPCA solver, resulting in a false detection. As an example, Fig. 7(a) shows the blood vessel and melanin particles in five consecutive *en face* images, and Figs. 7(d) and 7(f), respectively, show the false blood vessels extracted by RPCA and short-time RPCA methods. But it can be seen that the number of false detections of the short-time RPCA is less than that of the RPCA. Note that the melanin particles

TABLE II
F-MEASURE SCORES OF BLOOD VESSEL DETECTION METHODS (DIFFERENCE SHOWN IN PARENTHESIS)

Subvolume Index	Short-Time RPCA	Modified AD-OCTA	cmOCT	RPCA
1	0.5329	0.4753 (−0.0576)	0.4265 (−0.1064)	0.4821 (−0.0507)
2	0.6749	0.6562 (−0.0187)	0.6258 (−0.0491)	0.5966 (−0.0783)
3	0.4684	0.4904 (+0.0220)	0.2856 (−0.1828)	0.3477 (−0.1207)
4	0.6104	0.5832 (−0.0272)	0.6681 (+0.0577)	0.5447 (−0.0656)
5	0.7352	0.6409 (−0.0943)	0.7267 (−0.0085)	0.6807 (−0.0545)
6	0.4758	0.3136 (−0.1622)	0.4360 (−0.0398)	0.4661 (−0.0096)
7	0.8472	0.8079 (−0.0392)	0.5954 (−0.2518)	0.7721 (−0.0751)
8	0.6955	0.5485 (−0.1470)	0.2862 (−0.4094)	0.6905 (−0.0050)
9	0.6537	0.3227 (−0.3310)	0.2601 (−0.3936)	0.6921 (+0.0384)
10	0.7847	0.8094 (+0.0247)	0.7934 (+0.0087)	0.6961 (−0.0886)
11	0.7263	0.6654 (−0.0608)	0.5751 (−0.1512)	0.7593 (+0.0330)
12	0.7692	0.5414 (−0.2278)	0.5374 (−0.2317)	0.7371 (−0.0321)
13	0.5247	0.3049 (−0.2198)	0.2018 (−0.3228)	0.4621 (−0.0626)
14	0.4706	0.4645 (−0.0061)	0.1326 (−0.3380)	0.3546 (−0.1160)
15	0.4516	0.2490 (−0.2026)	0.1181 (−0.3335)	0.4528 (+0.0012)
Mean	0.6281	0.5249 (−0.1032)	0.4446 (−0.1835)	0.5823 (−0.0458)
<i>p</i> -value of paired sample t-test of the difference with respect to short-time RPCA		0.0021	0.0004	0.0028
Statistically significant		Yes	Yes	Yes

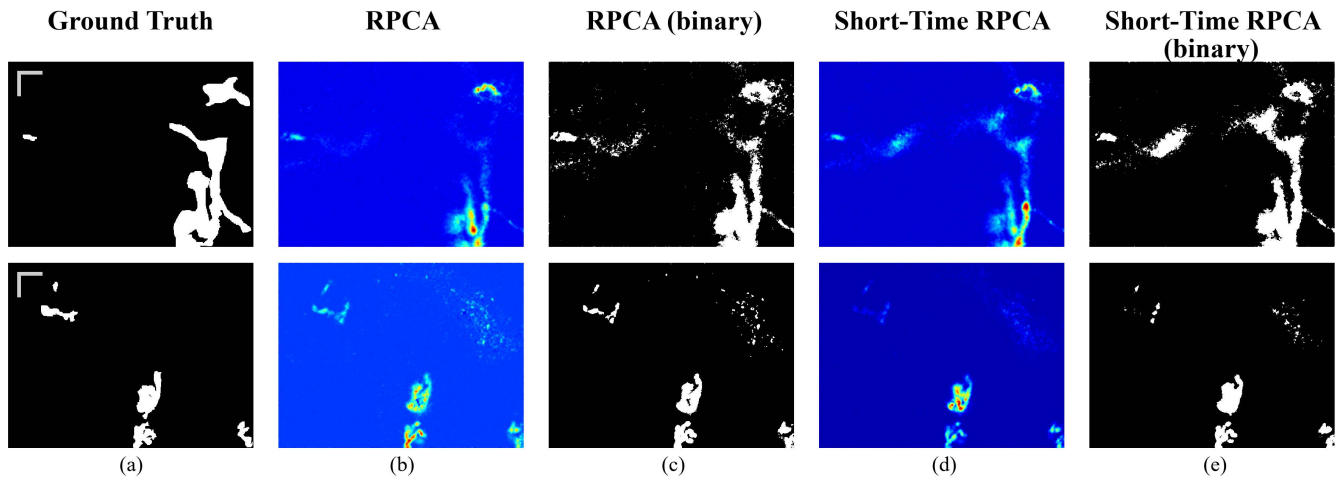


Fig. 9. Results for Subvolumes 9 and 11. (a) Ground truth. The scale bar represents 30 μm . (b) Result of the RPCA method. (c) Binarized result of the RPCA method. (d) Result of the short-time RPCA method. (e) Binarized result of the short-time RPCA method.

in some subvolumes degrade the blood vessel detection. Incorporating additional cell size and shape priors to improve the performance of our method should be further explored in the future.

D. Comparison Based on Binary Blood Vessels

We binarized the blood vessel image of each method with 100 different threshold values and generated 100 binary images. Then, we selected the binary image with the maximum F-measure score as the binary blood vessel image. Fig. 8(a) shows the blood vessels labeled by a dermatologist. These images are considered the ground truth. Figs. 8(b) to 8(e), in order, show the binary blood vessels extracted by the modified AD-OCTA, the cmOCT, the RPCA, and the short-time RPCA methods. It can be seen that the binary blood vessels generated by the short-time RPCA are most similar to

the ground truth blood vessels and have fewer false positives than those by the RPCA.

Table II lists the F-measure of the four methods. Out of the fifteen subvolumes, the short-time RPCA outperforms the RPCA for 12 subvolumes and achieves the highest F-measure for nine subvolumes. However, in contrary to the expectation, the F-measure of the short-time RPCA is lower than the RPCA for Subvolumes 9 and 11. Therefore, we take a close look at the extracted blood vessel images shown in Fig. 9 for these two subvolumes. Comparing the result for Subvolume 9 in Fig. 9(c) and 9(e), we can see that the short-time RPCA produced more details than the RPCA, but it also misclassified more background pixels as blood vessel pixels. As a result, it has a lower F-measure. Likewise, comparing the result for Subvolume 11 shown in Fig. 9(c) and 9(e), we can see that the short-time RPCA made less false detections caused by

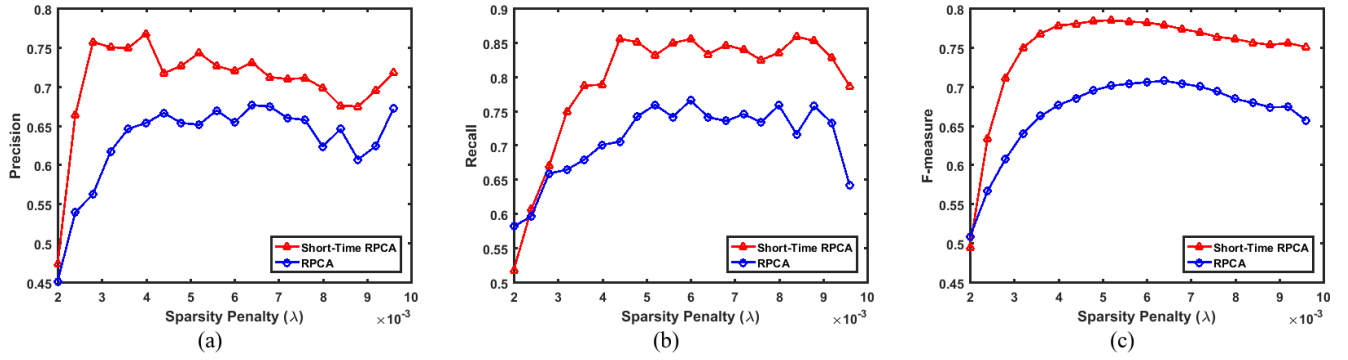


Fig. 10. Evaluation scores with respect to penalty factor λ of RPCA and short-time RPCA for Subvolume 10. (a) Precision. (b) Recall. (c) F-measure.

TABLE III
THE RANGE OF THE SPARSITY PENALTY FACTOR
FOR EACH SUBVOLUME

Subvolume Number	$\lambda (\times 10^{-3})$
1	3.6–6.0
2	3.2–6.0
3	2.8–5.2
4	4.4–9.6
5	4.0–8.0
6	4.4–8.0
7	2.0–8.8
8	2.0–8.4
9	4.0–8.0
10	3.2–9.6
11	2.0–4.8
12	3.2–7.2
13	4.8–8.8
14	3.6–6.4
15	2.4–8.0

melanin in the top right region of the image, at the cost of a lower detection rate for the blood vessel in the top left region of the image.

A paired sample t-test is a statistical procedure used to determine whether the mean difference between two sets of observations is zero [32]. We apply it to the F-measures in Table II. The resulting p -value is smaller than 0.05 in each case, meaning that there is significant difference between our method and any other method under comparison.

E. Sparsity Penalty Factor

To demonstrate how the sparsity penalty factor, or λ in (2), affects the performance of RPCA and short-time RPCA, we performed a separate experiment, where 20 different values of λ ranging from 2.0×10^{-3} to 9.6×10^{-3} were tested on a subvolume. Figs. 10(a) to 10(c), in order, show the change of the precision, recall, and F-measure scores with λ . For each subvolume, we can see subtle change of precision and recall within a range of λ , for which the F-measure is close to the maximum possible value. For example, the range is from 3.2×10^{-3} to 9.6×10^{-3} for the subvolume in Fig. 10. The short-time RPCA achieves the maximum F-measure at $\lambda = 4.8 \times 10^{-3}$, which is also within the range of λ for all

subvolumes (see Table III). Thus we adopted $\lambda = 4.8 \times 10^{-3}$ for the experiments described in Sections IV.C and IV.D.

F. Comparison of Computation Time

In terms of computational efficiency, our proposed short-time RPCA method outperforms the cmOCT and the RPCA methods. Specifically, the short-time RPCA takes 52 seconds on the average to process an FF-OCT subvolume, whereas the RPCA takes 109 seconds, the cmOCT takes 101 seconds, and the modified AD-OCTA takes 33 seconds. Note that our MATLAB code was run on a computer with Intel i5 2.4GHz CPU without GPU acceleration.

V. CONCLUSION

In this paper, we have described a short-time RPCA method for detecting blood vessels from FF-OCT data. The evaluation results should be taken with the fact in mind that the ground truth used in our experiments was labeled by only one dermatologist on six data volumes. As the work continues in the future, more data and subjects should be considered. However, it can be concluded at the present time that the short-time RPCA takes only half of the computation time of RPCA and that the performance of the proposed method is at least comparable to RPCA. Compared with the modified AD-OCTA and the cmOCT methods, the proposed method can better handle heavy speckle noise.

Currently, our short-time RPCA method is operated offline. It processes the FF-OCT data volume by volume. However, the Mirau-based FF-OCT system can be programmed to generate the data in a segment-by-segment manner. At its current speed, our method takes about one second to process a segment, about the same as the FF-OCT system. This is appealing because it is possible to integrate blood vessel detection with FF-OCT data acquisition in a pipeline.

Technical advances help expand the applicability of OCT to different skin diseases. For example, the finding of arborizing vessels can be a useful clue for early diagnosis of basal cell carcinoma, and a finer blood vasculature detection can enhance the diagnosis accuracy between actinic keratosis and basal cell carcinoma [35]. The computational efficiency of the proposed method is beneficial in speeding up the data acquisition and diagnosis process and adds additional value to the diagnostic capability of OCT.

ACKNOWLEDGEMENT

The authors wish to acknowledge dermatologist Dr. Jeng-Wei Tjiu for labeling the ground truth blood vessel images of all subvolumes of FF-OCT data used in the experiments.

REFERENCES

- [1] D. Huang *et al.*, "Optical coherence tomography," *Science*, vol. 254, no. 5035, pp. 1178–1181, 1991.
- [2] J. A. Izatt and M. A. Choma, "Theory of optical coherence tomography," in *Optical Coherence Tomography: Technology and Applications*, W. Drexler and J. G. Fujimoto, Eds. New York, NY, USA: Springer, 2008.
- [3] W. Drexler, M. Liu, A. Kumar, T. Kamali, A. Unterhuber, and R. A. Leitgeb, "Optical coherence tomography today: speed, contrast, and multimodality," *J. Biomed. Opt.*, vol. 19, no. 7, pp. 071412-1–071412-34, 2014.
- [4] T. E. de Carlo, A. Romano, N. K. Waheed, and J. S. Duker, "A review of optical coherence tomography angiography (OCTA)," *Int. J. Retina Vitreous*, vol. 1, no. 1, pp. 1–15, 2015.
- [5] C. Blatter *et al.*, "In situ structural and microangiographic assessment of human skin lesions with high-speed OCT," *Biomed. Opt. Exp.*, vol. 3, no. 10, pp. 2636–2646, 2012.
- [6] M. Mogensen, L. Thrane, T. M. Jørgensen, P. E. Andersen, and G. B. E. Jemec, "OCT imaging of skin cancer and other dermatological diseases," *J. Biophoton.*, vol. 2, nos. 6–7, pp. 442–451, 2009.
- [7] J. Qin, J. Jiang, L. An, D. Gareau, and R. K. Wang, "In vivo volumetric imaging of microcirculation within human skin under psoriatic conditions using optical microangiography," *Lasers Surg. Med.*, vol. 43, no. 2, pp. 122–129, 2011.
- [8] E. Dalimier and D. Salomon, "Full-field optical coherence tomography: A new technology for 3D high-resolution skin imaging," *Dermatology*, vol. 224, no. 1, pp. 84–92, 2012.
- [9] A. Dubois and A. C. Boccara, "Full-field optical coherence tomography," in *Optical Coherence Tomography: Technology and Applications*, W. Drexler and J. G. Fujimoto, Eds. New York, NY, USA: Springer, 2008.
- [10] C.-C. Tsai *et al.*, "Full-depth epidermis tomography using a Mirau-based full-field optical coherence tomography," *Biomed. Opt. Exp.*, vol. 5, no. 9, pp. 3001–3010, 2014.
- [11] M. Rajadhyaksha, M. Grossman, D. Esterowitz, and R. H. Webb, "In vivo confocal scanning laser microscopy of human skin: Melanin provides strong contrast," *J. Invest. Dermatol.*, vol. 104, no. 6, pp. 946–952, 1995.
- [12] R. A. Leitgeb, R. M. Werkmeister, C. Blatter, and L. Schmetterer, "Doppler optical coherence tomography," *Prog. Retinal Eye Res.*, vol. 41, no. 100, pp. 26–43, 2014.
- [13] S. Huang, M. Shen, D. Zhu, Q. Chen, C. Shi, Z. Chen, and F. Lu, "In vivo imaging of retinal hemodynamics with OCT angiography and Doppler OCT," *Biomed. Opt. Exp.*, vol. 7, no. 2, pp. 663–676, 2016.
- [14] A. Bouwens, D. Szigal, M. Szkulmowski, T. Bolmont, M. Wojtkowski, and T. Lasser, "Quantitative lateral and axial flow imaging with optical coherence microscopy and tomography," *Opt. Exp.*, vol. 21, no. 15, pp. 17711–17729, 2013.
- [15] D. M. Schwartz *et al.*, "Phase-variance optical coherence tomography: A technique for noninvasive angiography," *Ophthalmology*, vol. 121, no. 1, pp. 180–187, 2014.
- [16] J. Fingler, R. J. Zawadzki, J. S. Werner, D. Schwartz, and S. E. Fraser, "Volumetric microvascular imaging of human retina using optical coherence tomography with a novel motion contrast technique," *Opt. Exp.*, vol. 17, no. 24, pp. 22190–22200, 2009.
- [17] J. Enfield, E. Jonathan, and M. Leahy, "In vivo imaging of the microcirculation of the volar forearm using correlation mapping optical coherence tomography (cmOCT)," *Biomed. Opt. Exp.*, vol. 2, no. 5, pp. 1184–1193, 2011.
- [18] P. M. McNamara, M. Hrebresh, and M. J. Leahy, "In vivo full-field en face correlation mapping optical coherence tomography," *J. Biomed. Opt.*, vol. 18, no. 12, pp. 126008-1–126008-4, 2013.
- [19] Y. Jia *et al.*, "Split-spectrum amplitude-decorrelation angiography with optical coherence tomography," *Opt. Exp.*, vol. 20, no. 4, pp. 4710–4725, 2012.
- [20] M. S. Mahmud *et al.*, "Review of speckle and phase variance optical coherence tomography to visualize microvascular networks," *J. Biomed. Opt.*, vol. 18, no. 5, pp. 050901-1–050901-13, 2013.
- [21] I. Gorczynska, J. V. Migacz, R. J. Zawadzki, A. G. Capps, and J. S. Werner, "Comparison of amplitude-decorrelation, speckle-variance and phase-variance OCT angiography methods for imaging the human retina and choroid," *Biomed. Opt. Exp.*, vol. 7, no. 3, pp. 911–942, 2016.
- [22] E. Amaldi and V. Kann, "On the approximability of minimizing nonzero variables or unsatisfied relations in linear systems," *Theor. Comput. Sci.*, vol. 209, no. 1, pp. 237–260, 1998.
- [23] J. Wright, A. Ganesh, S. Rao, Y. Peng, and Y. Ma, "Robust principal component analysis: Exact recovery of corrupted low-rank matrices via convex optimization," in *Proc. Adv. Neural Inf. Process. Syst.*, 2009, pp. 2080–2088.
- [24] Z. Lin, R. Liu, and Z. Su, "Linearized alternating direction method with adaptive penalty for low-rank representation," in *Proc. Adv. Neural Inf. Process. Syst.*, 2011, pp. 612–620.
- [25] C. Guyon, T. Bouwmans, and E. Zahzah, "Foreground detection based on low-rank and block-sparse matrix decomposition," in *Proc. IEEE Int. Conf. Image Process.*, Orlando, FL, USA, Sep. 2012, pp. 1225–1228.
- [26] X. Zhou, C. Yang, and W. Yu, "Moving object detection by detecting contiguous outliers in the low-rank representation," *IEEE Trans. Pattern Anal. Mach. Intell.*, vol. 35, no. 3, pp. 597–610, Mar. 2013.
- [27] S. Javed, S. Andrews, T. Bouwmans, and S. K. Jung, "OR-PCA with dynamic feature selection for robust background subtraction," in *Proc. 30th ACM/SIGAPP Symp. Appl. Comput.*, 2015, pp. 86–91.
- [28] T. Bouwmans and E. H. Zahzah, "Robust PCA via principal component pursuit: A review for a comparative evaluation in video surveillance," *Comput. Vis. Image Understand.*, vol. 122, pp. 22–34, May 2014.
- [29] P.-H. Lee, C.-C. Chan, S.-L. Huang, A. Chen, and H. H. Chen, "Blood vessel extraction from OCT data by short-time RPCA," in *Proc. IEEE Int. Conf. Image Process.*, Phoenix, AZ, USA, Sep. 2016, pp. 394–398.
- [30] L. A. Matveev *et al.*, "Hybrid M-mode-like OCT imaging of three-dimensional microvasculature in vivo using reference-free processing of complex valued B-scans," *Opt. Lett.*, vol. 40, no. 7, pp. 1472–1475, 2015.
- [31] P. M. Kulkarni *et al.*, "Algorithms for improved 3-D reconstruction of live mammalian embryo vasculature from optical coherence tomography data," *Quant. Imag. Med. Surg.*, vol. 5, no. 1, pp. 125–135, 2015.
- [32] J. A. Rice, *Mathematical Statistics and Data Analysis*, 3rd ed. Belmont, CA, USA: Duxbury Advanced, 2006.
- [33] C.-L. Chen and R. K. Wang, "Optical coherence tomography based angiography [Invited]," *Biomed. Opt. Exp.*, vol. 8, no. 2, pp. 1056–1082, 2017.
- [34] N. Le, S. Song, Q. Zhang, and R. K. Wang, "Robust principal component analysis in optical micro-angiography," *Quant. Imag. Med. Surg.*, vol. 7, no. 6, pp. 654–667, 2017.
- [35] M. Ulrich *et al.*, "Dynamic optical coherence tomography in dermatology," *Dermatology*, vol. 232, no. 3, pp. 298–311, 2016.